

Spin-dependent Klein tunneling in graphene: Role of Rashba spin-orbit coupling

Ming-Hao Liu (劉明豪), Jan Bundesmann, and Klaus Richter
Institut für Theoretische Physik, Universität Regensburg, D-93040 Regensburg, Germany
 (Dated: December 5, 2011)

Within an effective Dirac theory the low-energy dispersions of monolayer graphene in the presence of Rashba spin-orbit coupling and spin-degenerate bilayer graphene are described by formally identical expressions. We explore implications of this correspondence for transport by choosing chiral tunneling through pn and pn junctions as a concrete example. A real-space Green's function formalism based on a tight-binding model is adopted to perform the ballistic transport calculations, which cover and confirm previous theoretical results based on the Dirac theory. Chiral tunneling in monolayer graphene in the presence of Rashba coupling is shown to indeed behave like in bilayer graphene. Combined effects of a forbidden normal transmission and spin separation are observed within the single-band $n \leftrightarrow p$ transmission regime. The former comes from real-spin conservation, in analogy with pseudospin conservation in bilayer graphene, while the latter arises from the intrinsic spin-Hall mechanism of the Rashba coupling.

PACS numbers: 72.80.Vp, 72.25.-b, 73.23.-b, 73.40.Gk

I. INTRODUCTION

After the first successful isolation of monolayer graphene (MLG) was announced,¹ intriguing properties based on its low-energy excitation that mimics massless, gapless, and chiral Dirac fermions were intensively investigated.^{2,3} Spin-orbit coupling (SOC), on the other hand, is the key ingredient of semiconductor spintronics^{4,5} that was undergoing a rapid development before the rise of graphene.⁶ The question about the role of SOC effects in graphene then naturally emerged, including the proposal of graphene as a topological insulator,⁷ which attracted the attention of various first-principles-based studies.⁸⁻¹⁰

SOC in MLG includes an intrinsic and an extrinsic term. The former reflects the inherent asymmetry of electron hopping between next nearest neighbors,⁷ i.e., a generalization of Haldane's model.¹¹ The latter is induced by the electric field perpendicular to the graphene plane, which can be externally controlled, and resembles the Rashba model^{12,13} for the two-dimensional electron gas. Agreement has been achieved, based on first-principles calculations,^{9,10} that the intrinsic SOC term opens a gap of the order of $2\lambda_I \approx 24 \mu\text{eV}$, while the Rashba SOC removes the spin degeneracy and creates a spin-splitting $2\lambda_R$ at the K and K' points that has a linear dependence on an external electric field E with the slope of about $100 \mu\text{eV}$ per $\text{V}/\text{\AA}$ of E . Under a strong gate voltage, the Rashba coupling may in principle dominate the intrinsic SOC in MLG.^{9,10}

The low-energy spectrum of MLG plus the Rashba coupling (MLG+R) was derived by Rashba,¹⁴ based on the Kane-Mele model,⁷ i.e., an effective Dirac Hamiltonian. An earlier work by one of us¹⁵ started with a tight-binding model (TBM) and obtained an equivalent form of the low-energy expansion,¹⁶

$$E_{\text{MLG+R}}(\mathbf{q}) \approx \mu \frac{1}{2} \left[\sqrt{(3t_R)^2 + (3ta \cdot \mathbf{q})^2} + \nu (3t_R) \right], \quad (1)$$

which also agrees with expressions given in Refs. 9 and 10 when $\lambda_I = 0$. Here $\mu, \nu = \pm 1$ are band indices, t and t_R are nearest-neighbor kinetic and Rashba hopping parameters,

respectively, $a \approx 1.42 \text{\AA}$ is the bonding length, and $\mathbf{q} = K + \delta\mathbf{k}$ with $|\delta\mathbf{k}|a \ll 1$. Recall for comparison the low-energy spectrum of bilayer graphene (BLG),^{2,17}

$$E_{\text{BLG}}(\mathbf{q}) \approx \mu \frac{1}{2} \left(\sqrt{\gamma_1^2 + (3ta \cdot \mathbf{q})^2} + \nu \gamma_1 \right), \quad (2)$$

where γ_1 is the nearest-neighbor hopping between the two graphene layers. Note that the next nearest-neighbor interlayer hoppings γ_3 and γ_4 do not influence the band dispersion near K . The completely different mechanisms of (i) pseudospin coupling between carriers from the two graphene layers of BLG through interlayer hopping γ_1 and (ii) real-spin coupling between up and down spins within MLG through Rashba hopping t_R happen to lead to an identical mathematical form in Eqs. (1) and (2) that can be clearly mapped onto each other.^{18,19} with $\gamma_1 \leftrightarrow 3t_R$ as sketched in Fig. 1. This unambiguously implies that low-energy physics in MLG+R and BLG should behave similarly.

In this paper we tackle the question of whether the transport in MLG+R behaves as in BLG by choosing the issue of Klein tunneling^{2,3,20,21} (or, in general, chiral tunneling) as a concrete example. Chiral tunneling in graphene has been shown to exhibit completely different behavior in MLG and BLG based on the Dirac theory.²² Tunneling at normal incidence in MLG shows a suppression of backscattering, which resembles the original Klein paradox in relativistic quantum

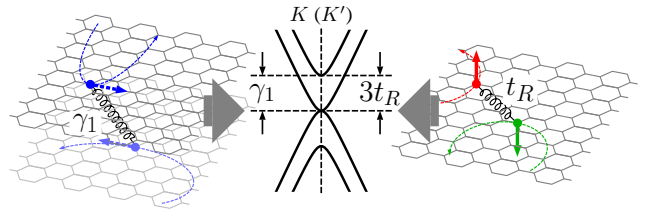


FIG. 1. (Color online) Schematic of the pseudospin coupling through γ_1 in BLG (left panel) and real-spin coupling through t_R in MLG (right), which lead to an identical low-energy dispersion near K and K' .

electrodynamics²³ and hence the name Klein tunneling, while in BLG it shows a perfect reflection, which is strictly speaking a consequence of forbidden interband transition also due to the chiral nature of graphene. The theoretical discussion of chiral tunneling so far focuses mainly on spin-independent tunneling through pn and pnp junctions,^{21,22,24–30} while SOC effects are less discussed.^{18,31–33} In addition, the relevant theoretical understanding so far is based on Dirac theory, which is valid only for the Fermi level close to the charge neutrality point and allows only to consider certain relatively simple systems. A recent study discussing the interplay between the Aharonov-Bohm effect and Klein tunneling in graphene, started with a TBM,³⁴ but the nanoribbon type of the leads used in that work may have edge effects included that can be very different from the bulk properties of graphene. A more transparent theoretical study of chiral tunneling in graphene directly bridging the analytical Dirac theory and the numerical TBM computation is so far missing and deserves consideration.

In the present work, we re-treat this issue of chiral tunneling in graphene based on the TBM and show a unified description, allowing for a broad range of geometries and complementing the existing results based on the Dirac theory. Straightforward generalization to the case of MLG+R reveals a spin-dependent tunneling behavior in close analogy with that in BLG, with the role of pseudospin in BLG replaced by real-spin in MLG+R. Specifically, a combined behavior of spin-Hall-based spin separation and suppression of normal transmission will be shown.

This paper is organized as follows. In Sec. II we briefly summarize the theoretical formalism applied in the present calculation, namely, real-space Green’s function formalism in noninteracting bulk graphene. In Sec. III we show our TBM results including the consistency with the Dirac theory, a direct comparison between BLG and MLG+R, and a deeper discussion of the MLG+R case. We review also briefly the recent experimental progress on the Rashba spin splitting and Klein tunneling in graphene in Sec. IV, and finally conclude in Sec. V.

II. FORMALISM

A. Tight-binding model for “bulk” graphene

We choose the TBM for describing the electronic properties of graphene, which is a well established way to treat graphene numerically. For spin-degenerate MLG, the Hamiltonian reads

$$\mathcal{H}_{\text{MLG}} = \sum_i V_i c_i^\dagger c_i - t \sum_{\langle i,j \rangle} c_i^\dagger c_j, \quad (3)$$

where the operator c_i^\dagger (c_i) creates (annihilates) an electron at site i (including both sublattices A and B). The first sum in Eq. (3) runs over all the atomic sites in the considered region with on-site potential V_i , and the second sum runs over all the pairs of neighboring atomic orbitals $\langle i,j \rangle$ with kinetic

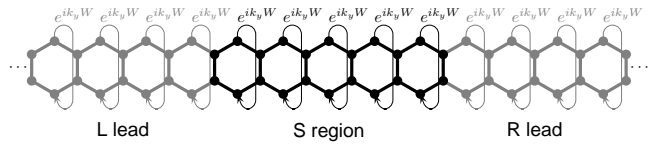


FIG. 2. Schematic of a minimum tight-binding model that simulates a bulk MLG up to nearest neighbor hoppings. Further nearest neighbor hoppings can be accounted for by enlarging the transverse periodicity W .

hopping parameter t (≈ 3 eV). The next nearest neighbor kinetic hopping term, usually characterized by $t' \approx 0.1t$, can be added in Eq. (3) but will not be considered in the present work due to the minor role it plays in the bulk transport properties for low-energy excitation.

Spin-orbit interactions can be incorporated into the TBM by altering the spin-dependent hopping between nearest and next-nearest neighbors,^{7,35} modifying Eq. (3) as

$$\mathcal{H}_{\text{MLG+R}} = \sum_i V_i \sigma^0 c_i^\dagger c_i + \sum_{\langle i,j \rangle} c_i^\dagger [-t\sigma^0 + it_R(\vec{\sigma} \times \mathbf{d}_{ij})_z] c_j. \quad (4)$$

Here σ^0 is the 2×2 identity matrix, t_R is the Rashba spin-orbit hopping parameter, \mathbf{d}_{ij} is the unit vector pointing from site j to i , and $\vec{\sigma} = (\sigma^x, \sigma^y, \sigma^z)$ is the vector of (real-) spin Pauli matrices. We take into account only the extrinsic SOC and neglect the intrinsic term that is usually much weaker, in order to highlight the role of the Rashba SOC.

For spin-degenerate BLG, we consider

$$\mathcal{H}_{\text{BLG}} = \sum_{m=1,2} \mathcal{H}_{\text{MLG}}^{(m)} - \gamma_1 \sum_j (b_{2,j}^\dagger a_{1,j} + \text{H.c.}), \quad (5)$$

where $\mathcal{H}_{\text{MLG}}^{(m)}$ is \mathcal{H}_{MLG} given by Eq. (3) of the m th graphene layer, $a_{m,j}$ ($b_{m,j}$) annihilates an electron on sublattice A (B) in layer $m = 1, 2$ at unit cell j (that contains two sublattice sites belonging to A and B), and the interlayer coupling strength $\gamma_1 \approx 0.4$ eV corresponds to the nearest neighbor hopping between the two MLG layers. Further interlayer hopping terms,² $-\gamma_4 \sum_j (a_{2,j}^\dagger a_{1,j} + b_{2,j}^\dagger b_{1,j} + \text{H.c.})$ and $-\gamma_3 \sum_j (a_{2,j}^\dagger b_{1,j} + \text{H.c.})$, are not considered in the present calculation, since they do not influence the low-energy excitation. Throughout the presentation of the numerical results in Sec. III, the kinetic hopping parameters will be fixed at $t = 3$ eV and $\gamma_1 = 0.4$ eV, while the value of the Rashba hopping parameter t_R depends on the context.

For the simulation of bulk graphene we impose periodic boundary conditions on nanoribbons of width W . This is done via modifying the hopping between atomic sites connected through the periodic boundary conditions by a Bloch phase factor $e^{ik_B W}$ with a Bloch momentum k_B , as schematically shown for MLG in Fig. 2. At the same time the Bloch momentum is the component of the electron’s momentum perpendicular to the nanoribbon. To be consistent with the literature related to Klein tunneling based on the Dirac theory, in Sec. III we will refer to the Bloch momentum as k_y .

B. Brief summary of real-space Green's function formalism

We consider open systems connected to the outer world by two leads (see Fig. 2). According to the real-space Green's function formalism³⁶ we numerically calculate the Green's functions of our system,

$$G_S^{r/a} = [E - H_S - \Sigma^{r/a} \pm i\eta]^{-1}, \quad (6)$$

where the self-energies of the leads ($\Sigma^{r/a} = \Sigma_L^{r/a} + \Sigma_R^{r/a}$) reflect the fact that our system is open. The powerful recipe constructed in Ref. 37 for graphene handles a lead as a semi-infinite repetition of unit cells and allows for incorporating any kind of lattice structure and one-body interaction such as SOCs. The transmission probability for an electron travelling from lead L to lead R is given by the Fisher-Lee relation^{36,37}

$$T_{RL} = \text{Tr}(\Gamma_L G_S^r \Gamma_R F_S^a), \quad (7)$$

where the trace is done with respect to the lattice sites. The spectral matrix functions $\Gamma_{L/R}$ are given by the lead self-energies as $\Gamma_{L/R} = i(\Sigma_{L/R}^r - \Sigma_{L/R}^a)$.

For a given Bloch momentum k_y and a given Fermi energy E_F [subject to a Fermi wave vector k_F via Eq. (1) for MLG+R or Eq. (2) for BLG], the incoming propagation angle ϕ of the electron wave can be defined as $\phi = \sin^{-1}(k_y/k_F)$. The angle-dependent transmission function $T(\phi)$ is obtained from Eq. (7), which can be generalized to a spin-resolved version.³⁸

III. TRANSPORT RESULTS

In this section we present numerical results of our tight-binding transport calculations. We first show the consistency of our tight-binding calculations with the existing effective Dirac theory in Sec. III A. A direct comparison between BLG and MLG+R will then be shown in Sec. III B. Finally, Sec. III C is devoted to MLG+R for pn junctions, in particular the role of Rashba SOC for chiral tunneling.

A. Consistency with Dirac theory

We first consider tunneling in graphene without SOC and confirm existing results, limited to low energy excitations, by our tight-binding calculations. We pick two pioneering theoretical works to demonstrate the consistency explicitly. Consistency with recent works of tunneling in graphene heterojunctions in the presence of SOC^{18,31} has also been checked, but is not explicitly shown here.

1. Chiral tunneling in MLG vs BLG

Tunneling in MLG and BLG behaves quite differently as mentioned in Sec. I and pointed out by Katsnelson *et al.*²² For comparison we consider a barrier of width $D = 100$ nm as in Ref. 22 for both MLG and BLG [see Figs. 3(a) and 3(c)].

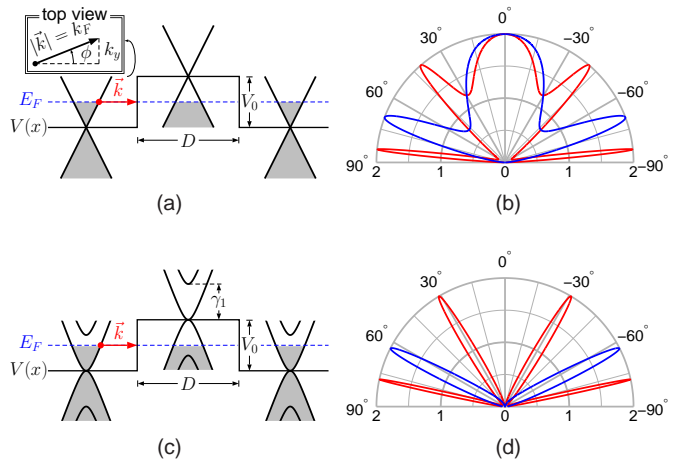


FIG. 3. (Color online) Tunneling through a barrier for (a), (b) MLG with $E_F = 83$ meV and (c), (d) BLG with $E_F = 17.6$ meV. In (b), red (light gray) and blue (dark gray) curves correspond to $V_0 = 200$ meV and $V_0 = 285$ meV, respectively. In (d), red (light gray) and blue (dark gray) curves correspond to $V_0 = 50$ meV and $V_0 = 103$ meV, respectively. In both cases the barrier width is $D = 100$ nm.

Note that in order to exactly match the barrier width, we set the bonding length $a = (4\sqrt{3})^{-1}$ nm, which differs from the realistic value of about 1.42 \AA by only less than 2%, so that the number of hexagons used here amounts to $4 \times [D]_{\text{nm}} = 400$.

The resulting transmission probabilities as a function of the incident angle ϕ are depicted in Figs. 3(b) and 3(d). They reproduce the results of Fig. 2 in Ref. 22 almost perfectly, if we choose slightly different E_F and V_0 , which the transmissions at finite angles are sensitive to. The remaining tiny difference between our TBM results and their Dirac theory results³⁹ simply reflects the basic difference between the two approaches: for graphene the effective Dirac theory is valid only for energies close to the Dirac point, while the TBM is suitable for the entire energy range.

Note that the maximal values of the transmission functions in Fig. 3 are 2, since the valley degeneracy is automatically incorporated in the tight-binding formalism. Later when we take spin also into account, the maximum of the transmission function will be 4. The transmission probabilities calculated by the Dirac theory always have their maximum of 1 due to the normalized incoming wave, unless a proper degeneracy factor is taken into account.

2. Klein tunneling in MLG: Sharp vs smooth interface

Tunneling in MLG through a pn junction exhibits probability one at normal incidence and is called Klein tunneling. In experiments, a graphene pn junction can be realized by using a backgate, which tunes the carrier density (and hence the Fermi level) globally, and a topgate that tunes locally the carrier density, equivalent to the potential step V_0 at the other side.⁴⁰ The carrier densities on the two sides can be controlled to be of

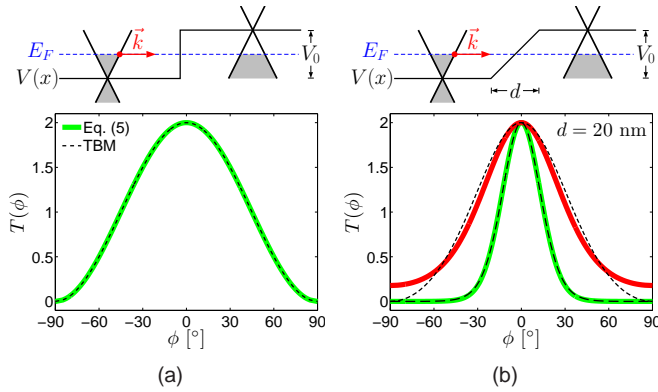


FIG. 4. (Color online) Klein tunneling in MLG through a pn junction with a (a) sharp and (b) smooth interface. (a) Comparison between TBM (dashed line) and Eq. (8) [solid green (gray)] showing perfect agreement ($E_F = 80$ meV). (b) Comparison between TBM (long and short dashed) and Eq. (9) [solid green (light gray) and red (dark gray)] for $k_F d \approx 6.16$ ($E_F = 200$ meV) and $k_F d \approx 1.54$ ($E_F = 50$ meV), respectively.

opposite signs, forming the pn junction. In between, however, the variation of the carrier density is never abrupt in reality. Cheianov and Fal'ko showed, based on the Dirac theory, that the interface of the pn junction actually matters.²⁴ They considered symmetric pn junctions (i.e., $V_0 = 2E_F$) with sharp and linearly smooth interfaces, which we briefly review and compare with our TBM results in the following.

a. Sharp interface For a symmetric pn junction with a sharp interface [see the schematic in Fig. 4(a)], the transmission probability as a function of ϕ was derived as²⁴

$$T(\phi) = \cos^2 \phi, \quad (8)$$

which does not depend on the potential step height. This surprisingly simple expression matches our TBM result always perfectly as long as $V_0 = 2E_F$, as shown in Fig. 4(a). However, asymmetric pn junctions with $V_0 \neq 2E_F$ cannot be handled by Eq. (8) but are straightforwardly treated by our calculation.

b. Smooth interface For symmetric pn junctions with a linearly varying region of width d [see the schematic in Fig. 4(b)], the analytical derivation for the transmission probability within the Dirac theory yields²⁴

$$T(\phi) = \exp\left(-\pi \frac{k_F d}{2} \sin^2 \phi\right) \quad (9)$$

for $k_F d \gg 1$.⁴¹ This formula, together with the validity criterion $k_F d \gg 1$, are tested by our tight-binding calculations shown in Fig. 4(b), where two sets of parameters are considered. For $k_F d \approx 6.16$ we find very good agreement with Eq. (9), while the result for $k_F d \approx 1.54$ exhibits noticeable deviations from the analytical prediction at large angles $|\phi|$. The smoothing function was assumed in their work as linear but the reality might be much more complicated, which is then not accessible by the Dirac theory but again straightforward

by our tight-binding calculation. Nevertheless, the exponential form of Eq. (9) is still a good description regardless of the actual form of the smoothing function, as we have numerically checked. What really matters is only the product $k_F d$.

B. pn junction: BLG vs MLG+R

We next show the direct correspondence between BLG and MLG+R by considering exactly the same potential barrier and incident Fermi energy as in Fig. 3(d) for BLG, and set $3t_R = \gamma_1 = 0.4$ eV for MLG+R here. (A discussion with weaker, realistic t_R will be continued in the next section.) The total transmission shown in Fig. 5 for MLG+R indeed resembles the curves in Fig. 3(d) for BLG, as expected due to the identical form of their low-energy dispersions (1) and (2). The most important feature of chiral tunneling in BLG, forbidden normal transmission, now appears also in the case of MLG+R. In BLG, $T(\phi = 0) = 0$ was understood as the consequence of pseudospin conservation. For MLG+R, $T(\phi = 0) = 0$ can be expected as the consequence of real-spin conservation. Indeed, this can be demonstrated by computing the nonequilibrium local spin density, which can be obtained from the lesser Green's function,⁴² considering two cases, $0 < E_F < 3t_R$ and $-3t_R < E_F < 0$, both with $k_y = 0$. Within this single-band transmission, the local spin densities for positive and negative E_F point to opposite directions, indicating that normal incidence transmission between n and p regions will be forbidden.

Next we discuss the spin-resolved transmission. The quantization axis is chosen as the out-of-plane direction, so that the transmission of, e.g., $T_{\downarrow\uparrow}$ means the probability of an incoming $+S_z$ electron ending up as an outgoing $-S_z$ one. Since the *incoming* angle dependence ϕ of the transmission probabilities are analyzed, we define $T_{\uparrow} = T_{\uparrow\uparrow} + T_{\downarrow\uparrow}$ as the trans-

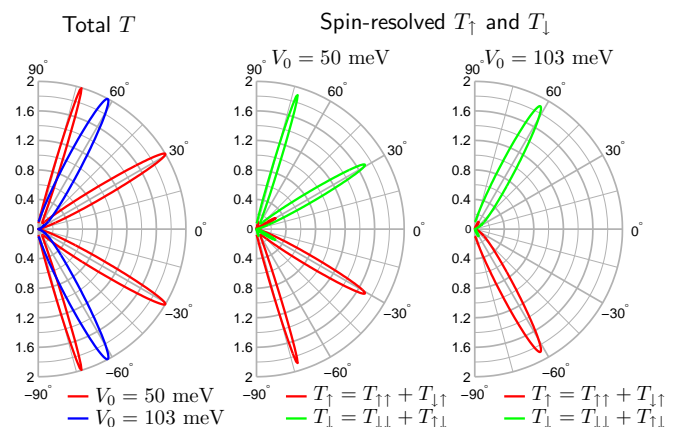


FIG. 5. (Color online) (a) Angle-resolved total transmission T for tunneling through a pn junction in MLG+R with the same barrier height V_0 , barrier width D , and Fermi energy E_F as used in Fig. 3(d) for BLG, and a substitution $3t_R = \gamma_1 = 0.4$ eV. (b) and (c) show spin-resolved transmission probabilities for $V_0 = 50$ meV and $V_0 = 103$ meV, respectively.

mission ability of the $+S_z$ electron (or \uparrow spin), and vice versa. (Alternatively, one can also analyze the *outgoing* angle dependence and define T_\uparrow as $T_{\uparrow\uparrow} + T_{\uparrow\downarrow}$, not used here. Either way, the total transmission $\sum_{\sigma,\sigma'=\uparrow,\downarrow} T_{\sigma\sigma'} = T_\uparrow + T_\downarrow = T$ is ensured.)

The choice of quantization axis z is not necessary but facilitates to relate the present spin-dependent tunneling in MLG with the issue of intrinsic spin-Hall effect previously discussed in semiconductors. The spin-resolved transmission curves shown in Fig. 5 exhibit opposite lateral preference of the \uparrow and \downarrow electron spins, which is an intrinsic spin-Hall mechanism due to the Rashba SOC. In a semiconductor two-dimensional electron gas, i.e., a continuous system rather than discrete as in the TBM, such an intrinsic spin-Hall deflection of opposite S_z electrons can be easily explained by the concept of a spin-orbit force based on the Heisenberg equation of motion,^{43,44}

$$\mathbf{F}_{so} = \frac{m}{i\hbar} \left[\frac{1}{i\hbar} [\mathbf{r}, \mathcal{H}], \mathcal{H} \right] = \frac{2m\alpha_R^2}{\hbar^3} (\mathbf{p} \times \mathbf{e}_z) \sigma^z. \quad (10)$$

Here $\mathcal{H} = p^2/2m + (\alpha_R/\hbar)(p_y\sigma^x - p_x\sigma^y)$ is the continuous two-dimensional Hamiltonian with Rashba SOC, \mathbf{r} and \mathbf{p} are the position and momentum operators, α_R is the Rashba coupling parameter (rather than the hopping one, t_R), and σ^z is the sign of the S_z spin component. The T_\uparrow and T_\downarrow curves shown in Fig. 5 therefore reveal a combined effect of forbidden normal transmission due to conservation of real-spin and the intrinsic spin-Hall deflection that can be understood by Eq. (10).

A few remarks are clue before we move on. To connect BLG with MLG+R we put $3t_R = \gamma_1 = 0.4\text{ eV}$, which is apparently far from reality. In general the Rashba splitting induced by electrical gating is roughly of or less than the order of $100\ \mu\text{eV}$ (see Sec. IV). Fermi energy lying within this splitting, which is also of our main interest, projects to a much shorter Fermi wave vector k_F , leading to a much longer d up to a few or a few tens of microns in order for $k_F d \gg 1$ to be valid. This implies that the influence of the interface on the tunneling in MLG+R is normally negligible, unless d is that long. In addition, tunneling through a pn junction will also require a long barrier width D for electrons subject to such a short k_F ; otherwise, the barrier is merely a weak perturbation to the electron due to its long Fermi wave length. Based on these remarks, we will focus in the next section only pn junctions in MLG+R with a reasonable Rashba hopping parameter.

C. pn junction in MLG+R

In the following we demonstrate in detail the role of Rashba SOC in tunneling through a potential step in MLG+R. The Rashba hopping parameter will be fixed to $t_R = 30\ \mu\text{eV}$ and the Fermi energy in most cases to $E_F = 2t_R$, which lies within the spin-orbit splitting $3t_R$ (see Fig. 1).

1. Normal incidence

We begin with the case of normal incidence, $k_y = 0$. In Sec. III B we have discussed the one-band transmission selection rule, i.e., $n \leftrightarrow p$ transmission is forbidden. The transmission from the left side at Fermi energy $0 < E_F < 3t_R$ to the right side with potential V_0 is expected to be zero whenever a single-band $n \rightarrow p$ transmission is attempted. Indeed, as shown in Fig. 6, a zero transmission gap of T as a function of V_0 is found. The gap lies in the interval of $E_F < V_0 < E_F + 3t_R$, corresponding to the single-band $n \rightarrow p$ transmission. Note that contrary to the valley-valve effect in zigzag nanoribbons,⁴⁵⁻⁴⁷ the gap shown here arises solely due to a bulk property.

2. Angle- and spin-resolved transmission

We proceed with angle- and spin-resolved transmission and consider first the trivial case with $E_F = 0.5\text{ meV}$ well above the Rashba splitting $3t_R = 90\ \mu\text{eV}$, as shown in Fig. 7. In this case the maximum of $T = T_\uparrow + T_\downarrow$ is 4 since two spin subbands and two valleys are involved in transport. The total transmission curve resembles the expected $\cos^2\phi$ behavior as discussed in Sec. III A 2, showing that the Rashba effect plays only a minor role. The spin-resolved T_\uparrow and T_\downarrow curves differ only slightly at $|\phi| = \sin^{-1}(k_F^{\text{in}}/k_F^{\text{out}}) \approx 56^\circ$, where k_F^{in} and k_F^{out} are the inner and outer radius of the two concentric Fermi circles, respectively. Tunneling in BLG with E_F well above γ_1 behaves similarly, i.e., the interlayer coupling γ_1 in BLG no longer plays an important role in the process of chiral tunneling when the transport occurs at $E_F \gg \gamma_1$, as we have numerically checked. In other words, the chiral tunneling in BLG with $E_F \gg \gamma_1$ and in MLG+R with $E_F \gg 3t_R$ recovers the Klein tunneling behavior as in MLG.

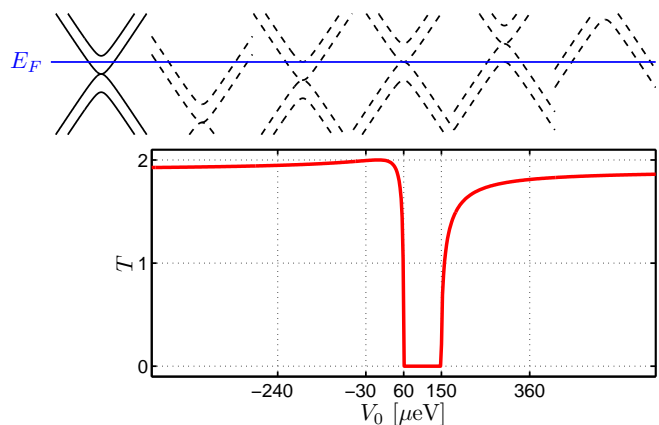


FIG. 6. (Color online) Transmission T at normal incidence ($k_y = 0$) as a function of potential step height V_0 for tunneling through a pn junction in MLG+R. The left-most solid band diagram above the main panel corresponds to the in-coming n side. The five ticks on the V_0 -axis correspond to the above five dashed band diagrams for the out-going side.

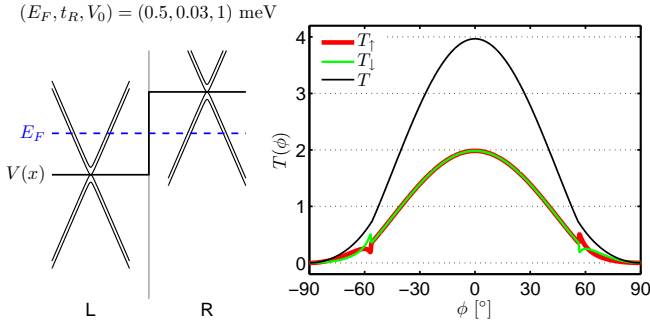


FIG. 7. (Color online) Angular dependence of total (T) and spin-resolved (T_\uparrow and T_\downarrow) transmissions for $E_F = 0.5$ meV well above the Rashba splitting $3t_R = 90 \mu\text{eV}$.

Of particular interest is the nontrivial case with $|E_F| < 3t_R$. As a test, we first consider $V_0 = 0$ as shown in Fig. 8(a). In the absence of the potential step, the total transmission function T reaches its maximum of 2 (one spin subband times valley degeneracy of two) for any angle ϕ , as it should. The opposite lateral deflection tendency of the \uparrow and \downarrow spins is again clearly seen and can be explained based on Eq. (10) as discussed in Sec. III B.

The most important case is that of Fermi energy $E_F \in (0, 3t_R)$ and potential height $V_0 \in (E_F, E_F + 3t_R)$. A specific example with $V_0 = 100 \mu\text{eV}$ is shown in Fig. 8(b), which exhibits the combined effect of the forbidden normal transmission [$T(\phi = 0) = 0$] and spin-Hall deflection. The number of high transmission peaks is always two.⁴⁸ Compared to the previous trivial case ($E_F > 3t_R$, Fig. 7) where T_\uparrow and T_\downarrow do not significantly differ, the separation of the opposite \uparrow and \downarrow spins is distinctly enhanced. Whether this could be a new type of intrinsic spin-Hall mechanism in graphene deserves a

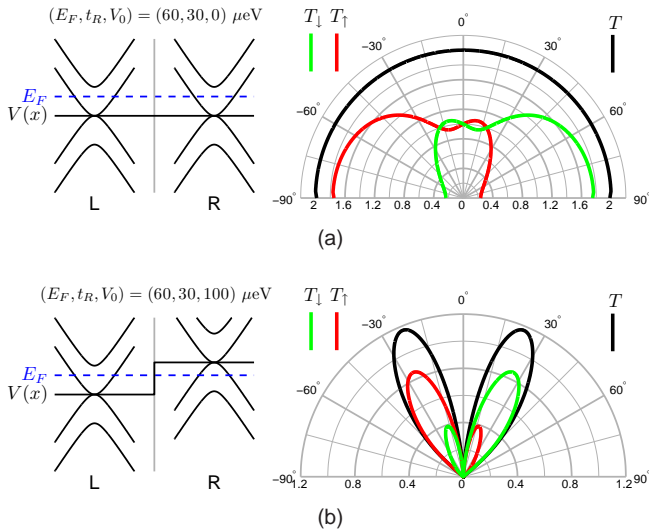


FIG. 8. (Color online) Angular dependence of total and spin-resolved transmissions through a pn junction in MLG+R with (a) zero potential and (b) finite potential. Parameters used are given above.

further investigation, and is left as a possible future direction.

We summarize the discussion of angle- and spin-resolved transmission by mapping $T(\phi, V_0)$ in Fig. 9. Four different transport regimes can be identified:

$V_0 < 0$: Single n band to single/multiple n band(s) transmission regime.

$0 < V_0 < E_F$: Single n band to single n band transmission regime; distinct spin-resolved T_\uparrow and T_\downarrow , and high total T limited by a critical angle $\phi_c = \sin^{-1}(k_F^R/k_F)$, where k_F^R is the Fermi wave vector in the outgoing (right) region.

$E_F < V_0 < E_F + 3t_R$: Single n band to single p band transmission regime; combined effects of forbidden normal transmission and spin-Hall deviation.

$V_0 > E_F + 3t_R$: Single n band to multiple p bands transmission regime.

Note that a vertical scan in Fig. 9 at $\phi = 0$ corresponds to Fig. 6, and horizontal scans at $V_0 = 0$ and $V_0 = 100 \mu\text{eV}$ to Figs. 8(a) and 8(b), respectively. These four regimes will be helpful in the following discussion of conductance.

3. Integrated conductance

Finally, we calculate the conductance of the pn junction in MLG+R by integrating $T(\phi)$, or equivalently, $T(k_y)$, with respect to the transverse Bloch momentum,

$$G = \frac{e^2/h}{2k_F} \int_{-k_F}^{k_F} T(k_y) dk_y, \quad (11)$$

where the prefactor ensures the maximal value of the Landauer-Büttiker type ballistic conductance to be e^2/h times the maximal number of modes.³⁶ We compare the conductance of the pn junction in MLG ($t_R = 0$) and in MLG+R ($t_R = 30 \mu\text{eV}$) as a function of the potential step height V_0 , as shown in Fig. 10. Since the Fermi level is fixed to $E_F = 60 \mu\text{eV}$ for both cases, the transport for $t_R = 0$ will involve two spin and two valley degeneracies, leading to the maximal G of $4e^2/h$, while in the case of $t_R = 30 \mu\text{eV}$ only one spin subband is projected, leading to the maximal G of $2e^2/h$. The maximal G occurs always at $V_0 = 0$ that corresponds to an ungated clean bulk graphene. Zero conductance, on the other hand, occurs at $V_0 = E_F$ since no states at the out-going region are available at this charge neutrality point.

Different transmission regimes can be distinguished based on our previous discussion for Fig. 9. For $V_0 \in [0, 60] \mu\text{eV}$ ($n \rightarrow n$ transmission), the rise of V_0 shrinks the Fermi circle at the out-going region and hence introduces a critical transverse momentum, outside which the transmission is suppressed due to the lack of out-going states. The critical transverse momentum reduces linearly with V_0 for MLG due to the linear dispersion. The conductance G , Eq. (11), therefore reduces also linearly with V_0 . In the presence of the Rashba

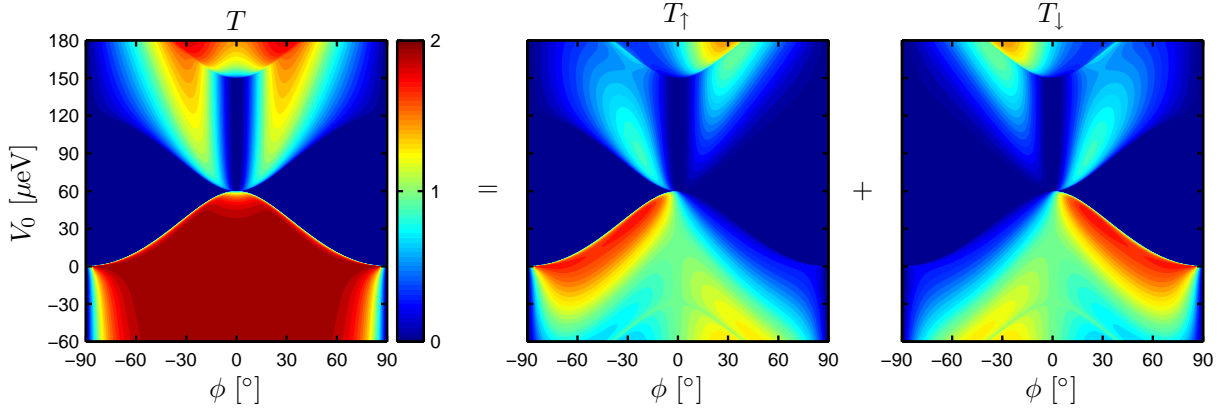


FIG. 9. (Color online) Transmission through a pn junction in MLG+R as a function of incident angle ϕ and potential step height V_0 . Four transmission regimes can be distinguished: (i) $V_0 < 0$, (ii) $0 < V_0 < E_F$, (iii) $E_F < V_0 < E_F + 3t_R$, and (iv) $V_0 > E_F + 3t_R$, with $E_F = 60 \mu\text{eV}$ and $3t_R = 90 \mu\text{eV}$.

SOC, the low-energy dispersion becomes quadratic, and so does the reduction of G with V_0 in MLG+R.

For $V_0 \in [60, 150] \mu\text{eV}$ ($n \rightarrow p$ transmission), the conductance of MLG rises faster than that of MLG+R, possibly due to the help of Klein tunneling. At $V_0 = 150 \mu\text{eV}$, a sudden jump (or a shoulder) occurs in the case of MLG+R since the second spin subband at the out-going region starts to participate in transport. This jump does not occur in the MLG case since both spin subbands are always degenerate. An earlier related work based on Dirac theory considered both intrinsic and Rashba SOC.¹⁸ The V_0 dependence of G for the Rashba dominated case in that work agrees well with the MLG+R curve shown in Fig. 10, including the shoulder.

IV. EXPERIMENTAL ASPECTS

A. Rashba spin splitting in graphene

Whereas the Rashba spin splitting in MLG induced by an applied electric field is in general in the order of no more than $100 \mu\text{eV}$, which is beyond the present resolution of

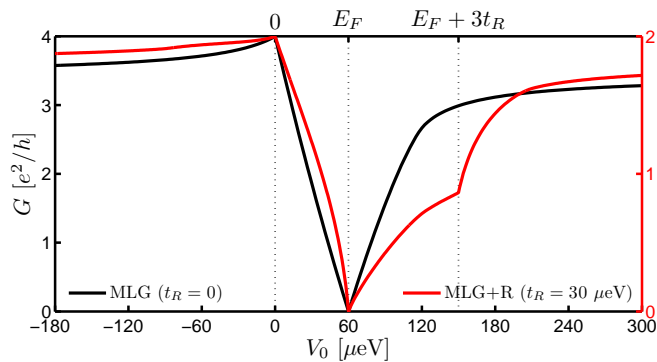


FIG. 10. (Color online) Integrated conductance of the ballistic pn junction in MLG with $t_R = 0$ and MLG+R with $t_R = 30 \mu\text{eV}$.

angle-resolved photoelectron spectroscopy (ARPES), direct experimental observation of the Rashba spin splitting at K and K' in agreement with the first-principles calculations^{9,10} is so far not reported. An earlier experiment on epitaxial graphene layers on a Ni(111) surface reported a large Rashba interaction⁴⁹ up to 225 meV but was soon questioned since the splitting might simply revealed a Zeeman type splitting due to the ferromagnetic nature of nickel.⁵⁰ An intercalated Au monolayer between the graphene layer and the Ni(111) substrate reduced the splitting to about 13 meV and was concluded as the Rashba effect on the π states supported by spin-resolved ARPES.⁵¹ However, the low-energy band structure of MLG+R at that time was not yet clear, and a simplified picture was adopted in the explanation of the measured spin splitting. In addition, transport properties of graphene based on metallic substrates can be difficult to isolate since a large bulk current will interfere as background.⁵²

Throughout the above calculations we have mostly focused on a rather weak Rashba hopping parameter $t_R = 30 \mu\text{eV}$, yielding a splitting at the K and K' points $3t_R = 90 \mu\text{eV}$, which is a realistic and rather conservative estimate for the gate-voltage-induced Rashba SOC strength. A recent proposal of impurity-induced SOC in graphene,⁵³ however, indicated that the coupling strength can be strongly enhanced by putting heavy adatoms⁵⁴ as well as by hydrogenation.^{53,55}

B. Klein tunneling in MLG

Indirect and direct experimental evidences of Klein tunneling in MLG have been reported recently.^{56,57} For detailed reviews, we refer to Refs. 2, 3, 20, 21, and 58. A very recent experiment on transport through a pn junction in MLG used an embedded local gate, which yields high quality ballistic transport and perfectly independent control of the local carrier density, as well as the feature of Klein tunneling.⁵⁹

Recall the $t_R = 0$ curve of conductance for MLG shown in Fig. 10. Overall, the conductance for $n \rightarrow n$ transmission with $V_0 < 0$ is always higher than that for $n \rightarrow p$ transmission

with $V_0 > E_F$. Even though Klein tunneling leads to perfect transmission at normal incidence in the latter case, the decay of T with incident angle eventually yields a lower conductance after integration. This feature has been agreed in recent experiments for pn and pnp junctions in MLG.^{40,56,57,59–63} The difference of the conductance, or equivalently the resistance, between the nn and np (or between pp and pn) in experiments is even more obvious possibly due to the smooth interface that leads to an exponentially decaying form of T ,²⁴ as we have reviewed and discussed in Sec. III A 2. In fact, for MLG we have numerically checked G for pn junctions with a smooth interface, which indeed can enhance the difference of G between the nn and np regimes.

Another interesting feature so far experimentally reported only in Refs. 57 and 59 is the Fabry-Perot oscillation of the conductance for pnp junctions due to the interference between the two interfaces of the central barrier. This feature requires the system to be ballistic and can be naturally revealed by our tight-binding transport calculation, which we will elaborate elsewhere in the future.

V. CONCLUSION AND OUTLOOK

In conclusion, we have employed tight-binding calculations to show that transport properties of MLG+R behave as BLG due to their identical form of the low-energy dispersion, choosing the chiral tunneling in pn and pnp junctions as a concrete example. Within single-band transmission, normal incidence transmission through a pn junction in BLG with $|E_F| < \gamma_1$ is forbidden as a consequence of pseudospin conservation,²² while in MLG+R with $|E_F| < 3t_R$ this forbidden transmission also occurs but as a consequence of real-spin conservation. In mapping the angle- and spin-resolved transmission for the MLG+R case, a combined effect of forbidden normal transmission and intrinsic spin-Hall deflection

is revealed [Fig. 8(b)]. Compared to the potential-free spin-Hall deflection case as shown in Fig. 8(a), where $T_\uparrow = T_\downarrow = 1$ at $\phi = 0$, the effect of the pn junction seems to force the up and down spins to separate since $T_\uparrow = T_\downarrow = 0$ at $\phi = 0$. The feature revealed in Fig. 8(b) may therefore suggest a new type of intrinsic spin-Hall mechanism in MLG.

Within multi-band transmission, however, the Rashba SOC in MLG no longer plays an important role when $|E_F| \gg 3t_R$ (Fig. 7). Likewise, the interlayer hopping γ_1 in BLG becomes unimportant when $|E_F| \gg \gamma_1$. Transport in both MLG+R with $|E_F| \gg 3t_R$ and BLG with $|E_F| \gg \gamma_1$ recovers to that in MLG, despite the usually very different energy scales of $3t_R$ and γ_1 . In view of the distinct transmission patterns in MLG+R with $|E_F| < 3t_R$ [Fig. 8(b)] and $|E_F| \gg 3t_R$ (Fig. 7), as an interesting conjecture for the BLG case one expects very different scattering regimes for $|E_F| < \gamma_1$ and $|E_F| \gg \gamma_1$. The former is well discussed in the literature and exhibits strong scattering [Fig. 3(d)] while the latter is less discussed and the scattering is expected to be strongly suppressed.

MLG and BLG are known to behave quite differently in general, in the sense of single-band transmission. Whereas turning MLG directly into BLG is in principle not possible, steering MLG to MLG+R can be achieved simply by gating, and therefore the effect of Rashba SOC provides a possibility to continuously change the MLG-like transport properties to BLG-like. We expect further transport properties to behave similarly in BLG and in MLG+R, such as the quantum Hall effect,⁶⁴ as was also noted by Rashba.¹⁴

ACKNOWLEDGMENTS

We gratefully acknowledge Alexander von Humboldt Foundation (M.H.L.) and Deutsche Forschungsgemeinschaft (within SFB689) (J.B. and K.R.) for financial support.

¹ K. S. Novoselov, A. K. Geim, S. V. Morozov, D. Jiang, Y. Zhang, S. V. Dubonos, I. V. Grigorieva, and A. A. Firsov, *Science* **306**, 666 (2004).
² A. H. Castro Neto, F. Guinea, N. M. R. Peres, K. S. Novoselov, and A. K. Geim, *Rev. Mod. Phys.* **81**, 109 (2009).
³ S. Das Sarma, S. Adam, E. H. Hwang, and E. Rossi, *Rev. Mod. Phys.* **83**, 407 (2011).
⁴ D. D. Awschalom, D. Loss, and N. Samarth, eds., *Semiconductor Spintronics and Quantum Computation* (Springer, Berlin, 2002).
⁵ I. Žutić, J. Fabian, and S. Das Sarma, *Rev. Mod. Phys.* **76**, 323 (2004).
⁶ A. K. Geim and K. S. Novoselov, *Nat. Mater.* **6**, 183 (2007).
⁷ C. L. Kane and E. J. Mele, *Phys. Rev. Lett.* **95**, 226801 (2005).
⁸ H. Min, J. E. Hill, N. A. Sinitsyn, B. R. Sahu, L. Kleinman, and A. H. MacDonald, *Phys. Rev. B* **74**, 165310 (2006).
⁹ M. Gmitra, S. Konschuh, C. Ertler, C. Ambrosch-Draxl, and J. Fabian, *Phys. Rev. B* **80**, 235431 (2009).
¹⁰ S. Abdelouahed, A. Ernst, J. Henk, I. V. Maznichenko, and I. Mertig, *Phys. Rev. B* **82**, 125424 (2010).
¹¹ F. D. M. Haldane, *Phys. Rev. Lett.* **61**, 2015 (1988).

¹² E. I. Rashba, *Sov. Phys. Solid State* **2**, 1109 (1960).
¹³ Y. A. Bychkov and E. I. Rashba, *JETP Lett.* **39**, 78 (1984).
¹⁴ E. I. Rashba, *Phys. Rev. B* **79**, 161409(R) (2009).
¹⁵ M.-H. Liu and C.-R. Chang, *Phys. Rev. B* **80**, 241304(R) (2009).
¹⁶ Due to a minor difference in the definition of the Rashba coupling in the tight-binding Hamiltonian, the splitting $3t_R$ here corresponds, e.g., to λ in Ref. 14 and to $2\lambda_R$ in Ref. 9.
¹⁷ E. McCann and V. I. Fal'ko, *Phys. Rev. Lett.* **96**, 086805 (2006).
¹⁸ A. Yamakage, K. I. Imura, J. Cayssol, and Y. Kuramoto, *EPL* **87** (2009).
¹⁹ P. Rakyta, A. Kormányos, and J. Cserti, *Phys. Rev. B* **82**, 113405 (2010).
²⁰ C. W. J. Beenakker, *Rev. Mod. Phys.* **80**, 1337 (2008).
²¹ P. Allain and J. Fuchs, *The European Physical Journal B - Condensed Matter and Complex Systems* **83**, 301 (2011).
²² M. I. Katsnelson, K. S. Novoselov, and A. K. Geim, *Nature Physics* **2**, 620 (2006).
²³ O. Klein, *Zeitschrift für Physik* **53**, 157 (1929).
²⁴ V. V. Cheianov and V. I. Fal'ko, *Phys. Rev. B* **74**, 041403 (2006).
²⁵ L. M. Zhang and M. M. Fogler, *Phys. Rev. Lett.* **100**, 116804

- (2008).
- ²⁶ E. B. Sonin, Phys. Rev. B **79**, 195438 (2009).
- ²⁷ C. Bai, Y. Yang, and X. Zhang, Physica E: Low-dimensional Systems and Nanostructures **42**, 1431 (2010).
- ²⁸ E. Rossi, J. H. Bardarson, P. W. Brouwer, and S. Das Sarma, Phys. Rev. B **81**, 121408 (2010).
- ²⁹ J. M. Pereira Jr, F. M. Peeters, A. Chaves, and G. A. Farias, Semicond. Sci. Tech. **25**, 033002 (2010).
- ³⁰ T. Tudorovskiy, K. J. A. Reijnders, and M. I. Katsnelson, (2011), arXiv:1106.3042 [cond-mat.mes-hall].
- ³¹ D. Bercioux and A. De Martino, Phys. Rev. B **81**, 165410 (2010).
- ³² C. Bai, J. Wang, J. Tian, and Y. Yang, Physica E: Low-dimensional Systems and Nanostructures **43**, 207 (2010).
- ³³ M. Rataj and J. Barnaś, Appl. Phys. Lett. **99**, 162107 (2011).
- ³⁴ J. Schelter, D. Bohr, and B. Trauzettel, Phys. Rev. B **81**, 195441 (2010).
- ³⁵ S. Konschuh, M. Gmitra, and J. Fabian, Phys. Rev. B **82**, 245412 (2010).
- ³⁶ S. Datta, *Electronic Transport in Mesoscopic Systems* (Cambridge University Press, Cambridge, 1995).
- ³⁷ M. Wimmer, *Quantum transport in nanostructures: From computational concepts to spintronics in graphene and magnetic tunnel junctions*, Ph.D. thesis, Universität Regensburg (2008).
- ³⁸ B. K. Nikolić and R. L. Dragomirova, Semicond. Sci. Tech. **24**, 064006 (2009).
- ³⁹ The unity transmission peaks (except the 0° peaks for MLG) are shifted by less than 3° compared to Fig. 2 of Ref. 22.
- ⁴⁰ J. R. Williams, L. DiCarlo, and C. M. Marcus, Science **317**, 638 (2007).
- ⁴¹ Note that an additional factor of $1/2$ in the exponent of Eq. (9) as compared to the original formula given in Ref. 24 comes from the fact that the linear potential profile across the interface changes from $-V_0$ to V_0 in Ref. 24, but here from 0 to V_0 , i.e., k_F reduces to $k_F/2$.
- ⁴² B. K. Nikolić, L. P. Zarbo, and S. Souma, Phys. Rev. B **73**, 075303 (2006).
- ⁴³ J. Li, L. Hu, and S.-Q. Shen, Phys. Rev. B **71**, 241305 (2005).
- ⁴⁴ B. K. Nikolić, L. P. Zârbo, and S. Welack, Phys. Rev. B **72**, 075335 (2005).
- ⁴⁵ K. Wakabayashi and T. Aoki, Int. J. Mod. Phys. B **16**, 4897 (2002).
- ⁴⁶ A. Rycerz, J. Tworzydło, and C. W. J. Beenakker, Nat. Phys. **3**, 172 (2007).
- ⁴⁷ A. Cresti, G. Grosso, and G. P. Parravicini, Phys. Rev. B **77**, 233402 (2008).
- ⁴⁸ We have numerically checked that the double-peak feature of T_{tot} in the single-band $n \leftrightarrow p$ transmission regime shown in Fig. 8(b) still holds even if the intrinsic SOC is present, as long as the Rashba coupling dominates.
- ⁴⁹ Y. S. Dedkov, M. Fonin, U. Rüdiger, and C. Laubschat, Phys. Rev. Lett. **100**, 107602 (2008).
- ⁵⁰ O. Rader, A. Varykhalov, J. Sánchez-Barriga, D. Marchenko, A. Rybkin, and A. M. Shikin, Phys. Rev. Lett. **102**, 057602 (2009).
- ⁵¹ A. Varykhalov, J. Sanchez-Barriga, A. M. Shikin, C. Biswas, E. Vescovo, A. Rybkin, D. Marchenko, and O. Rader, Phys. Rev. Lett. **101**, 157601 (2008).
- ⁵² K. Yaji, Y. Ohtsubo, S. Hatta, H. Okuyama, K. Miyamoto, T. Okuda, A. Kimura, H. Namatame, M. Taniguchi, and T. Aruga, Nat. Comm. **1** (2010), 10.1038/ncomms1016.
- ⁵³ A. H. Castro Neto and F. Guinea, Phys. Rev. Lett. **103**, 026804 (2009).
- ⁵⁴ C. Weeks, J. Hu, J. Alicea, M. Franz, and R. Wu, (2011), arXiv:1104.3282 [cond-mat.mes-hall].
- ⁵⁵ D. C. Elias, R. R. Nair, T. M. G. Mohiuddin, S. V. Morozov, P. Blake, M. P. Halsall, A. C. Ferrari, D. W. Boukhvalov, M. I. Katsnelson, A. K. Geim, and K. S. Novoselov, Science **323**, 610 (2009).
- ⁵⁶ N. Stander, B. Huard, and D. Goldhaber-Gordon, Phys. Rev. Lett. **102**, 026807 (2009).
- ⁵⁷ A. F. Young and P. Kim, Nat. Phys. **5**, 222 (2009).
- ⁵⁸ A. F. Young and P. Kim, Annual Review of Condensed Matter Physics, **2**, 101 (2011).
- ⁵⁹ S.-G. Nam, D.-K. Ki, J. W. Park, Y. Kim, J. S. Kim, and H.-J. Lee, Nanotechnology **22**, 415203 (2011).
- ⁶⁰ B. Huard, J. A. Sulpizio, N. Stander, K. Todd, B. Yang, and D. Goldhaber-Gordon, Phys. Rev. Lett. **98**, 236803 (2007).
- ⁶¹ B. Özyilmaz, P. Jarillo-Herrero, D. Efetov, D. A. Abanin, L. S. Levitov, and P. Kim, Phys. Rev. Lett. **99**, 166804 (2007).
- ⁶² G. Liu, J. J. Velasco, W. Bao, and C. N. Lau, **92**, 203103 (2008).
- ⁶³ N. M. Gabor, J. C. W. Song, Q. Ma, N. L. Nair, T. Taychatanapat, K. Watanabe, T. Taniguchi, L. S. Levitov, and P. Jarillo-Herrero, Science **334**, 648 (2011).
- ⁶⁴ K. S. Novoselov, A. K. Geim, S. V. Morozov, D. Jiang, M. I. Katsnelson, I. V. Grigorieva, S. V. Dubonos, and A. A. Firsov, Nature **438**, 197 (2005).